Supplementary Information for

Microscopic Dynamics Underlying the Stress Relaxation of Arrested Soft Materials

Jake Song,[1,2] Qingteng Zhang,[3] Felipe de Quesada,[1] Mehedi H. Rizvi,[4] Joseph B. Tracy,[4] Jan Ilavsky,[3] Suresh Narayanan,[3] Emanuela del Gado,[5] Robert Leheny,[6] Niels Holten-Andersen*[1] and Gareth H. McKinley*[2]

[1]Department of Materials Science and Engineering and [2]Department of Mechanical Engineering, Massachusetts Institute of Technology
[3]X-ray Sciences Division, Argonne National Laboratory,
[4]Department of Materials Science and Engineering, North Caroline State University,
[5]Department of Physics, Georgetown University,
[6]Department of Physics and Astronomy, Johns Hopkins University.
Corresponding emails: holten@mit.edu, gareth@mit.edu

Table of Contents

Supplementary Figures

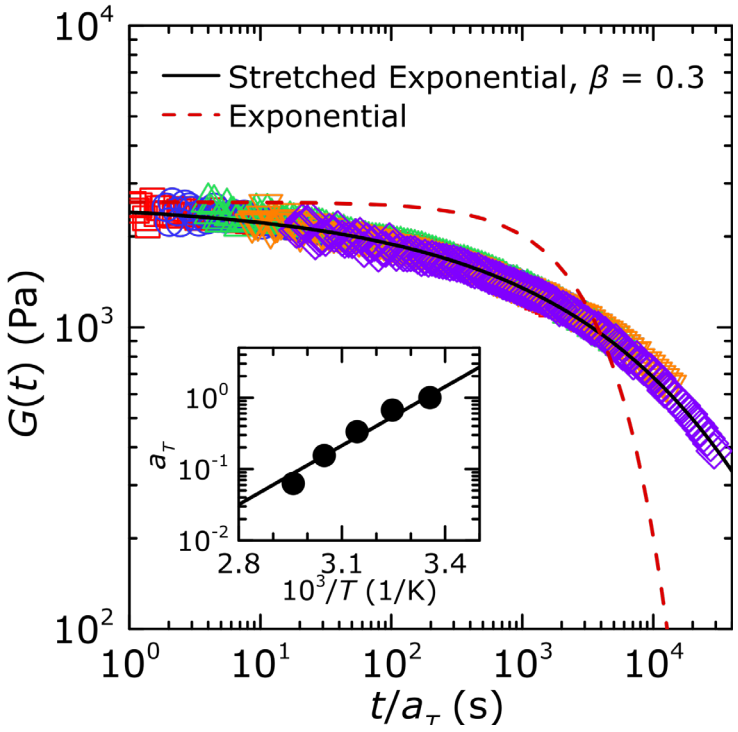

Figure S1. Time-temperature-superposition of the temperature-dependent $G(t)$ in Fig. 1B. Reference temperature $T_{ref} = 25^oC$. Solid line is the stretched exponential fit taken directly from the one used for $T = 25^oC$ in Fig. 1B. Dashed line shows an exponential function with the same relaxation time τ as the stretched exponential fit. Inset: Arrhenius plot of the shift factor a_T as a function of inverse temperature, yielding an activation energy of $E_A = 21.3\ kT$.

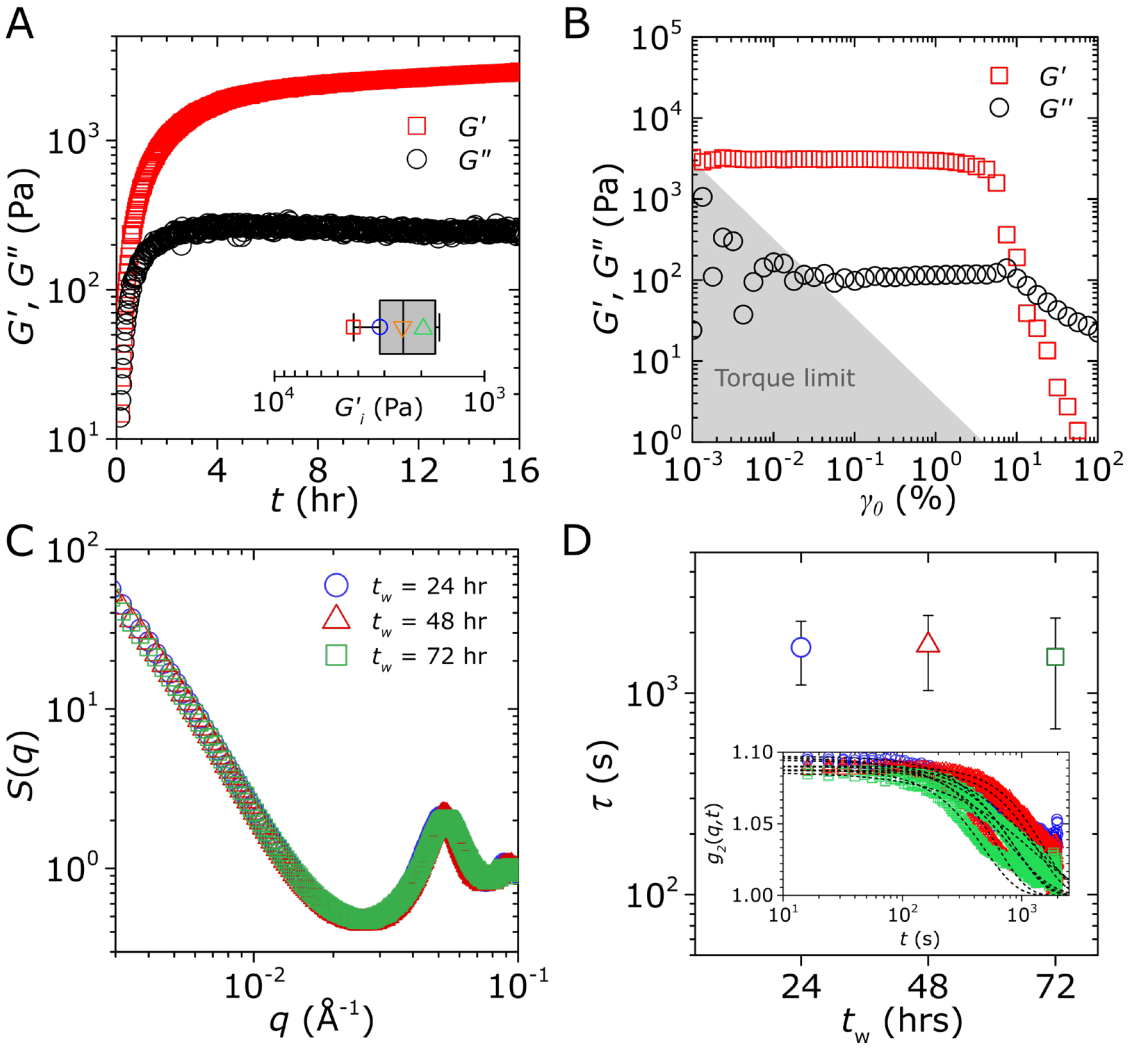

Figure S2. Supplementary characterization of the gelation kinetics and quiescent properties of the arrested gel. A) Gelation plot of the model system at $\phi_{NP} = 1.50$ %. Measurement of the storage modulus G' and loss modulus G'' during ligand exchange at $T = 55^oC$, probed at $\gamma_o = 0.1$ % and $\omega = 1$ rads^{-1}. (Inset) Statistical variation in the initial storage modulus G_i' of the final gel measured at $T = 25^oC$ (sample size of 7). The respective G_i' values used in the normalization of the data in Fig. 1C of the main manuscripts are shown as symbols (symbols corresponding to those in Fig. 1C). B) Amplitude sweep measurements for the model system at $\omega = 1$ rads^{-1} probed at $T = 25^oC$ after gelation. All stress relaxation experiments in Fig. 1B are conducted with step strains of $\gamma_o = 0.5$ %, well within the linear viscoelastic regime of the system. C) Structure factor $S(q)$ obtained from small-angle x-ray scattering performed on the gel system made via *in situ* gelation in a sealed capillary using the beamline setup for XPCS. $S(q)$ here is obtained by dividing the $I(q)$ by the hard-sphere model result (Fig. 2B). D) Relaxation time τ_m obtained from XPCS at different waiting times (same legend as Fig. C). All τ_m are obtained by applying the Siegert relation to three decay data per waiting time (see Inset). The colors of markers in the inset figures follow the colors of the main plot.

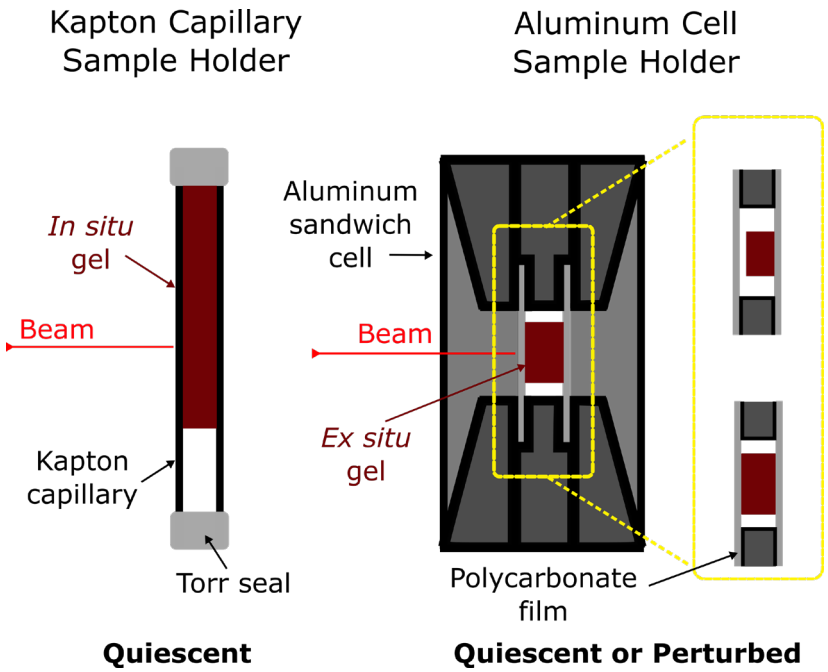

Figure S3. Illustration of the sample holders used in the study. For the capillary system, the material is gelled *in situ* in a sealed Kapton capillary. For the aluminum system, the materials are gelled *ex situ* in a sealed container, and then placed inside the aluminum cell (under-filled and filled, respectively).

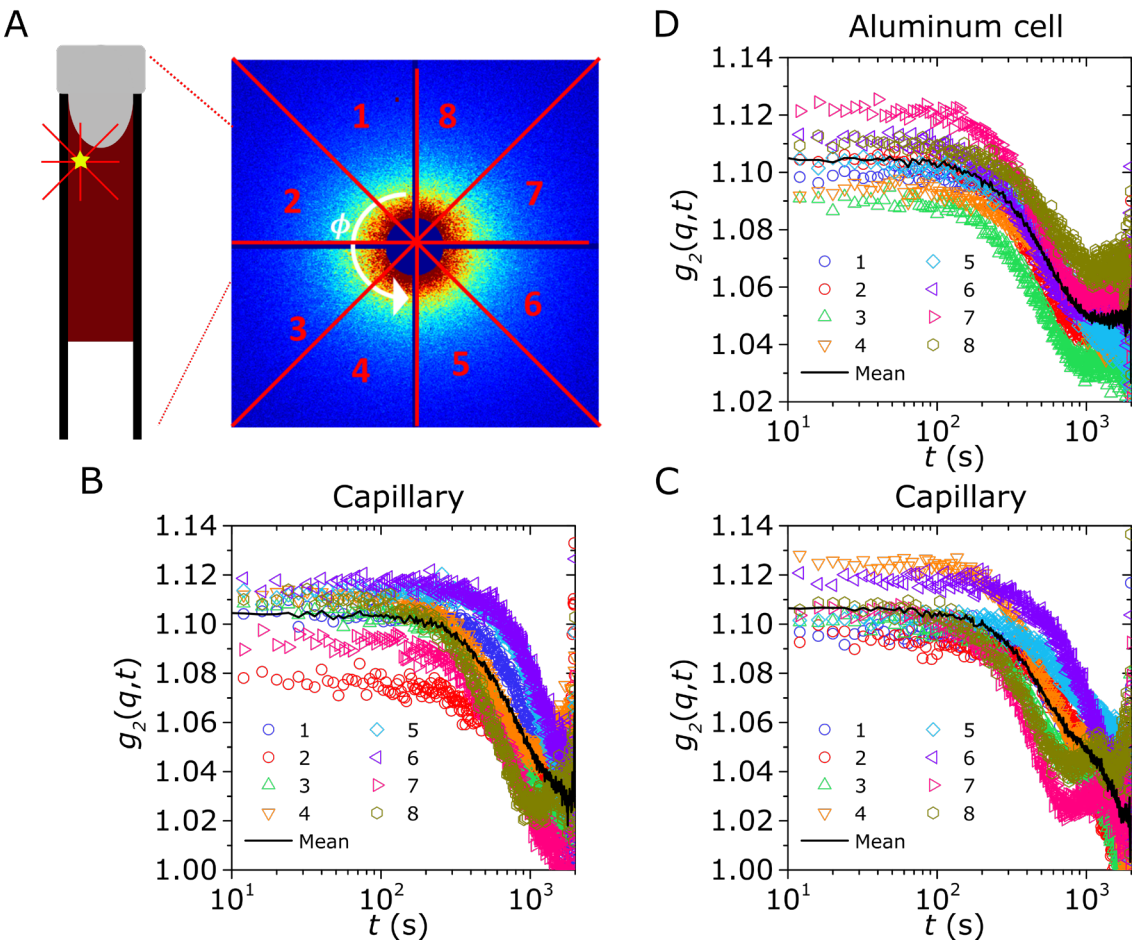

Figure S4. Second order correlation function $g_2(q,t)$ measured at $q = 0.0032$ Å^{-1} as a function of the azimuthal angle ϕ. A) In the capillary-gelled sample, we probe the top left of the capillary as shown, and divide the speckle pattern into 8 sectors (at $\phi = \pi/4$ increments). The ϕ-dependent correlation functions thus probe the microscopic dynamics of the gel at different directions. In this configuration, we can see that directions 2, 3, 7, and 8 are the most *confined* (by either the capillary walls or by the Torr seal), whereas directions 1, 4, 5, and 6 are less confined. These confinements are expected to generate additional internal stresses, and thus if the dynamics in Fig. 2C in the main text are caused by internal stresses, we expect a ϕ-dependency in the relaxation time (faster in the direction of greater confinement). B, C) Two representative ϕ-dependent correlation functions in the capillary configuration. The most notable trends are that, indeed, sectors 2, 3, 7, and 8 show faster correlation than sectors 1, 4, 5, and 6, thus confirming that internal stresses dictate microscopic relaxation times τ_m. The ensemble averaging of these disparate relaxation dynamics give rise to the tail of the relaxation shown (and not fitted to the Siegert relation) in Fig. 2C. D) Same ϕ-dependent analysis on the aluminum cell sample. Though spatial heterogeneities exist in terms of the contrast, the dynamics is generally similar and without obvious directional patterns, due to the multifaceted confinement experienced by the sample during gelation as well as loading.

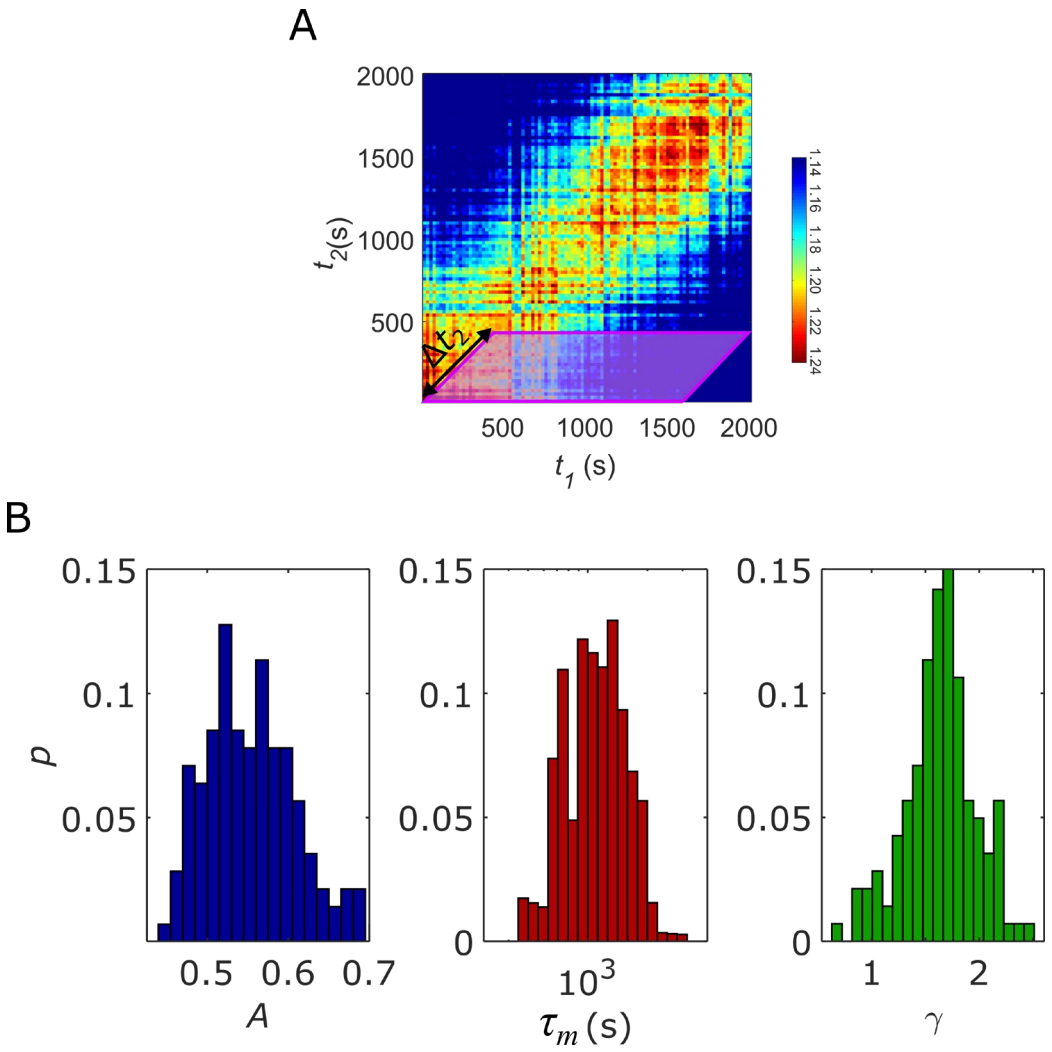

Figure S5. Statistical analysis of the 20 capillary experiments performed on the quiescent gel at $q = 0.0032$ Å^{-1}. A) To obtain even higher statistics, the two-time correlation C_I of each experiment was further binned by sections of $\Delta t_2 = 400$ s, and then correlations across t_1 were taken both in the forward and reverse temporal direction. An example of this is shown in the figure. Thus, approximately 10 $g_2(q, t, \Delta t_2)$ data were obtained per experiment, resulting in a total of 200 $g_2(q, t, \Delta t_2)$ data analyzed. B) Results of the statistical analysis on the $g_2(q, t, \Delta t_2)$ data. Mean values are the following: $A = 0.55 \pm 0.051$; $\tau_m = 1305 \pm 424\ s$; $\gamma = 1.635 \pm 0.33$. The distribution in the microscopic relaxation time τ_m appears to follow a lognormal distribution around the mean.

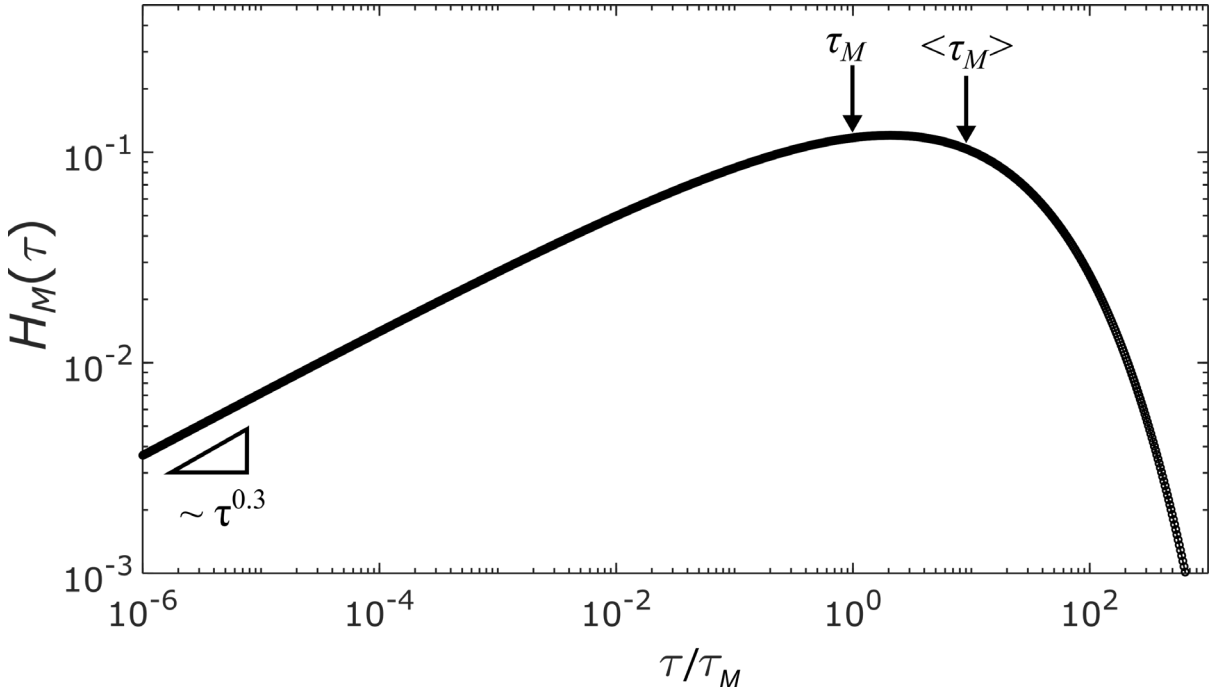

Figure S6. Continuous relaxation time spectrum $H_M(\tau)$ arising from a stretched exponential function (Eqn. 1) with $\beta = 0.3$. The exponent $\beta = 0.3$ is taken directly from the fits to the experimental data. The stretched exponential function is characterized by a heavy-tail distribution at short times (with a slope of β), and a mean relaxation time $\langle\tau_M\rangle$ (Eqn. 3 in the main text) which is higher than the fitted stress relaxation time τ_M (Eqn. 1). The spectrum function is obtained analytically through the Lindsey-Patterson relation[1] below.

$$H_M(\tau) = -\frac{\tau_M}{\pi\tau}\left[\sum_{k=0}^{\infty}\frac{(-1)^k}{k!}\sin(\pi\beta k)\Gamma(\beta k+1)\left(\frac{\tau}{\tau_M}\right)^{\beta k}\right]$$

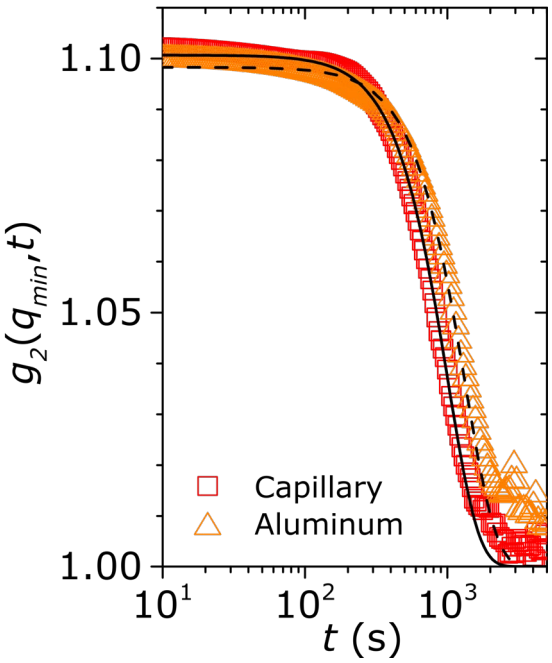

Figure S7. Comparison of the representative g_2 for quiescent systems gelled in a capillary configuration C (data shown in Fig. 4B of the main text) and in an aluminum cell configuration A. Fitting results to the Siegert relation (Eqn. 2 in the main text) with a ballistic decay exponent of $\gamma = 1.\dot{9}$ are shown as solid lines and dashed lines for the C and A configurations, respectively. As noted in the main text, the data presented here are t-q superposed, wherein data collected at $0.0032\ \text{Å}^{-1} \leq q \leq 0.010\ \text{Å}^{-1}$ are shifted to a reference wavevector of $q_{min} = 0.0032\ \text{Å}^{-1}$.

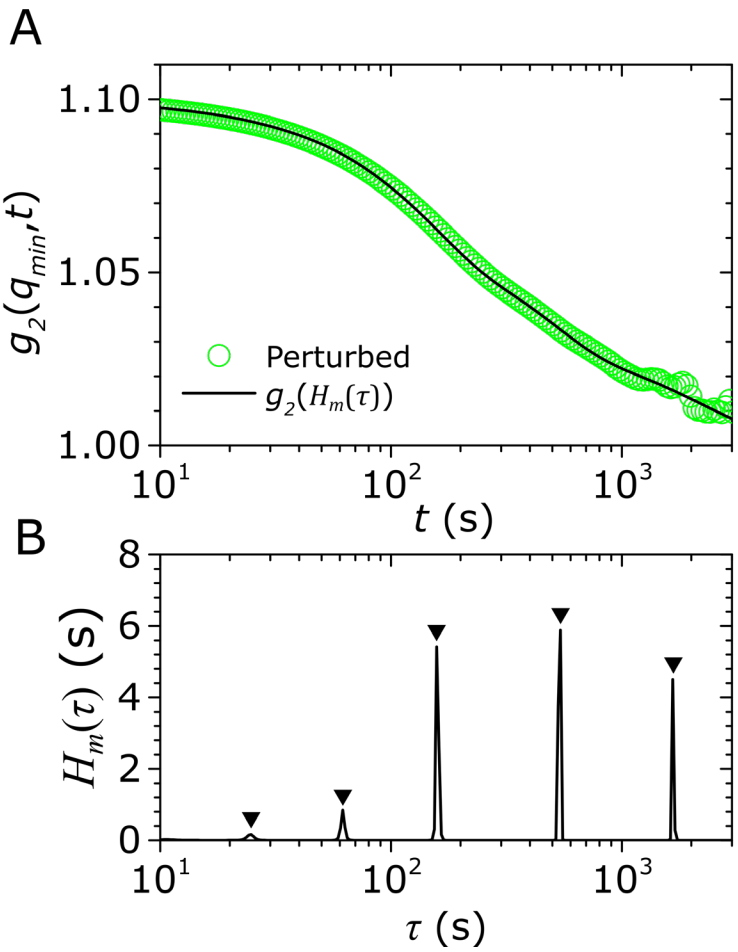

Figure S8. Representative example of the protocol for obtaining $H_m(\tau)$ shown on the perturbed system in Fig. 4B at $q_{min} = 0.0032$ Å^{-1}. Eqn. 4 is estimated via a regularization method (see Methods) which is applied to g_2 data in A) to obtain a discrete set of relaxation spectra in B). The regularization criterion is set to minimize the mean squared error. This results in the sharply peaked spectrum function shown in B). The peak values of this spectrum are recorded; an ensemble of these peak values is shown in Fig. 4C. The solid line in A) represents the back-calculated $g_2(q,t)$ from the derived relaxation spectrum $H_m(\tau)$ in B), showing good agreement with experimental data.

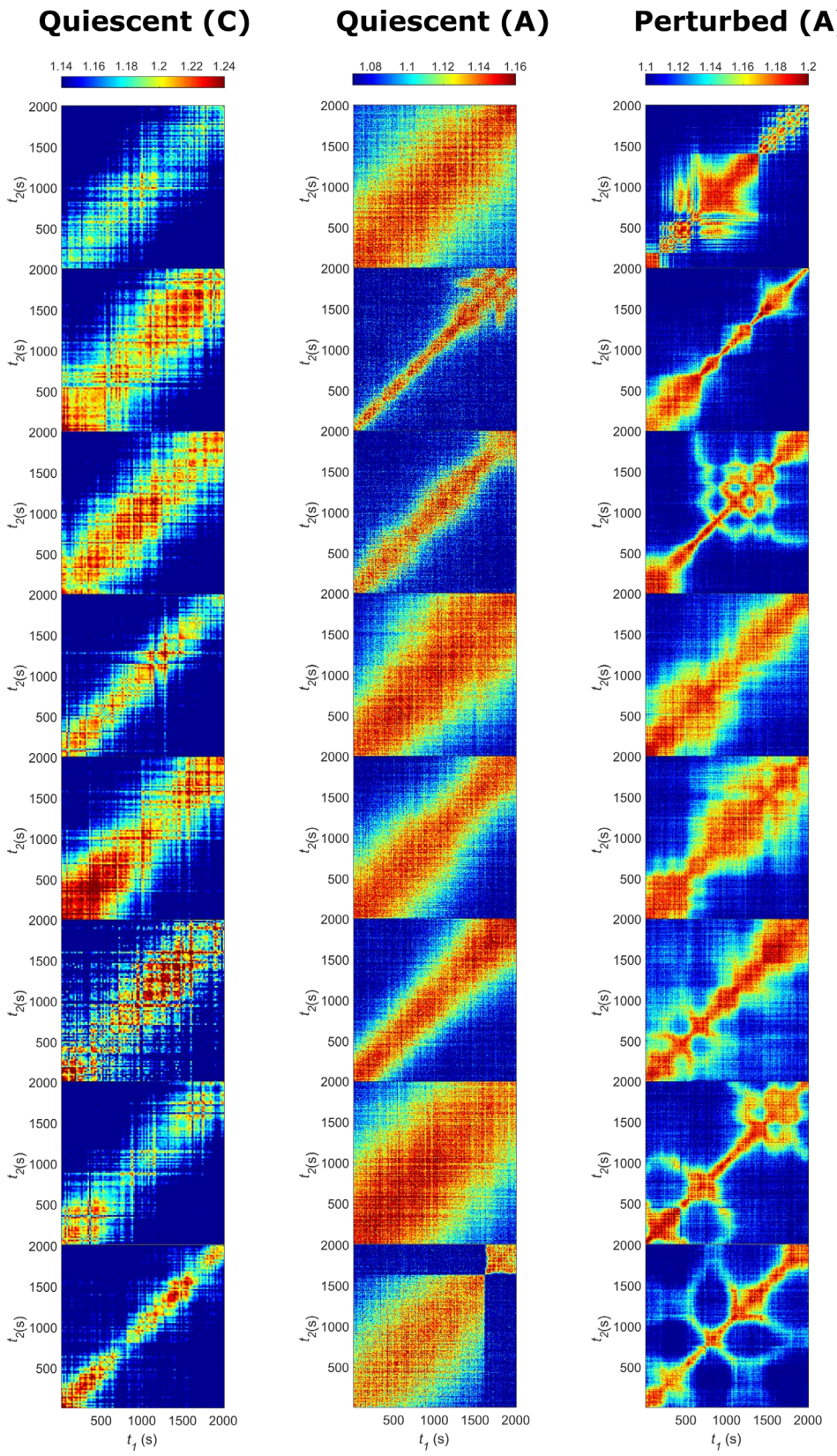

Figure S9. Larger ensemble of C_I for the quiescent state (C), quiescent state (A), and perturbed state (A) – sample holders are denoted in parentheses. All measurements are taken at $q_{min} = 0.0032\ \dot{A}^{-1}$. Differences in the width of the bands within each configuration arise from the fact that each experiment is done on a different local region (see Methods), thus reflecting the microstructural heterogeneities in the relaxation time of the system (see for example Fig. S5 for statistics of the quiescent capillary system). Each experiment done on a given configuration also shows some temporal heterogeneities, as shown by the thinning and thickening of the bands. This figure also shows that the aluminum cell (middle column) is less capable of producing a complete quiescent state compared to the capillary, evidenced by the presence of more temporal heterogeneities in the C_I. This is because the sample must be gelled *ex situ*; though care is taken to prepare the quiescent sample in the aluminum, the C_I, the loading process inevitably creates some mechanical perturbations. The relaxation dynamics that arise from the quiescent aluminum configuration is nevertheless similar to that which arises from the capillary configuration (see representative g_2 in Fig. S7 and statistics of relaxation modes in Fig. 4C).

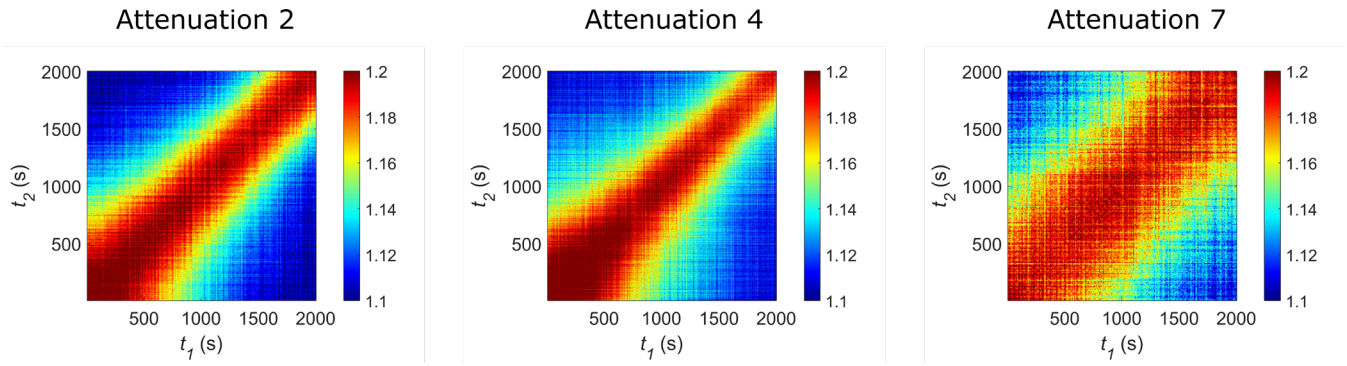

Figure S10. Representative two-time correlations C_I arising from trial experiments using different attenuation levels on the quiescent (A) sample at $T = 25$ °C and $q = 0.0032$ Å^{-1}. The attenuation level n signify reduction of the beam strength by a factor of 2^n. At lower attenuation levels, there is a distinct thinning of the two-time correlation bands, reflecting beam-induced damage and fluidization of the sample. We chose attenuation levels where such thinning behavior disappears for our experiments. We confirmed that the C_I bands of attenuation 7 were not affected by a competing effect between aging (which would thicken the bands) and beam-damage (which would thin the bands) by taking measurements of the system at three different waiting times: 24, 48, and 72 hours (the results of this are shown in Fig. S2D, and shows constant relaxation times obtained at different waiting times). The higher-attenuation plots also shows that intermittent dynamics which were observed in the mechanically-perturbed samples (Fig. 5B) are not observed from radiation damage.

Supplementary Tables

Table S1. Fitting parameters for USAXS measurements

Hard Sphere Model			**Unified Model**			
ϕ	Radius	Std. Dev	G	R_g (Å)	B	P
0.14	32.0	5.0	14470.6	1881.0	0.00011	2.7

Table S2. Fitting parameters for Fig. 2D and 3A at different configurations ($\tau_m(q) = Cq^{-v}$). C is related to the inverse of the generalized diffusion coefficient D_v.

Fig. 2D

$C(s/m^v)$	v
2.69×10^{10}	1.07

Fig. 3A

$\boldsymbol{T = 25\ ^oC}$		$\boldsymbol{T = 35\ ^oC}$		$\boldsymbol{T = 45\ ^oC}$		$\boldsymbol{T = 55\ ^oC}$	
$C(s/m^v)$	v	$C(s/m^v)$	v	$C(s/m^v)$	v	$C(s/m^v)$	v
3.6×10^5	1.25	2.9×10^5	1.31	2.9×10^6	0.96	1.6×10^6	1.04

Table S3. Fitting parameters for Arrhenius fit in Fig. 3C.

τ_0 (s)	$E_A(kT)$
3.2×10^{-5}	20.87

References

1. Lindsey, C.; Patterson, G., Detailed comparison of the Williams–Watts and Cole–Davidson functions. *The Journal Of Chemical Physics* **1980,** *73* (7), 3348-3357.